nature electronics

Article

https://doi.org/10.1038/s41928-024-01169-1

Efficient data processing using tunable entropy-stabilized oxide memristors

Received: 18 February 2023

Accepted: 18 April 2024

Published online: 20 May 2024

Check for updates

Sangmin Yoo[1,8], Sieun Chae[2,8], Tony Chiang[2], Matthew Webb[2], Tao Ma[3], Hanjong Paik[4], Yongmo Park[1], Logan Williams[2], Kazuki Nomoto[5], Huili G. Xing[5,6], Susan Trolier-McKinstry[7], Emmanouil Kioupakis[2], John T. Heron[2] ✉ & Wei D. Lu[1] ✉

Memristive devices are of potential use in a range of computing applications. However, many of these devices are based on amorphous materials, where systematic control of the switching dynamics is challenging. Here we report tunable and stable memristors based on an entropy-stabilized oxide. We use single-crystalline (Mg,Co,Ni,Cu,Zn)O films grown on an epitaxial bottom electrode. By adjusting the magnesium composition (X_{Mg} = 0.11–0.27) of the entropy-stabilized oxide films, a range of internal time constants (159–278 ns) for the switching process can be obtained. We use the memristors to create a reservoir computing network that classifies time-series input data and show that the reservoir computing system, which has tunable reservoirs, offers better classification accuracy and energy efficiency than previous reservoir system implementations.

A memristor[1–3] is a two-terminal device with an electrical resistance that can be modulated by electrical inputs. The devices can be used to colocate compute and memory functions, improving system throughput and energy efficiency while providing a high integration density[4–8]. So far, several memristor-based prototypes have been developed for tasks such as neural network inference and training[2,3,6–10]. The programmed conductance values of devices are often used for multiply-and-accumulate applications. However, the (short-term and long-term) internal dynamics of memristors have also been used to directly process temporal data for tasks such as time-series analysis and prediction[11–15].

The switching dynamics of a memristor are determined by how the storage material is physically reconfigured in response to electrical input[16]. Various memristive materials and their switching mechanisms have been studied, with efforts focused on amorphous oxides such as TaO_x (ref. 17–20), NbO_x (ref. 21), WO_x (refs. 22,23) and TiO_2 (ref. 3), whose resistivity states are determined by an electric field-driven redistribution of oxygen vacancies. However, challenges associated with the stochasticity during the filament growth process and the limited tunability of the material composition have restricted the development of physical dynamics that can be customized for specific applications.

Entropy-stabilized oxides (ESOs) are a new class of materials in which a uniform solid solution of typically five or more different cations is stabilized in a single phase due to the configurational entropy overcoming a competing enthalpy[24]. Local compositional variations render a local structural disorder (Fig. 1a) that can modify the material's fundamental structure–property relationships. ESOs are thus a promising material for achieving targeted functional properties through fine-tuning of alloy composition[25].

In this Article, we report the development of memristors formed through the epitaxial integration of single-crystalline ESO films on a single-crystal oxide electrode. The devices offer tunable and stable resistive switching (RS) dynamics that are derived from composition control. We use single-crystalline (Mg,Co,Ni,Cu,Zn)O ESO films grown on an epitaxial bottom electrode, where a controlled trapped state forms over small changes in cation composition with associated

[1]Department of Electrical Engineering and Computer Science, University of Michigan, Ann Arbor, MI, USA. [2]Department of Materials Science and Engineering, University of Michigan, Ann Arbor, MI, USA. [3]Michigan Center for Materials Characterization, University of Michigan, Ann Arbor, MI, USA. [4]School of Electrical and Computer Engineering, University of Oklahoma, Norman, OK, USA. [5]School of Electrical and Computer Engineering, Cornell University, Ithaca, NY, USA. [6]Department of Materials Science and Engineering, Cornell University, Ithaca, NY, USA. [7]Department of Materials Science and Engineering and Materials Research Institute, The Pennsylvania State University, University Park, PA, USA. [8]These authors contributed equally: Sangmin Yoo, Sieun Chae. ✉e-mail: jtheron@umich.edu; wluee@umich.edu

https://doi.org/10.1038/s41928-024-01169-1

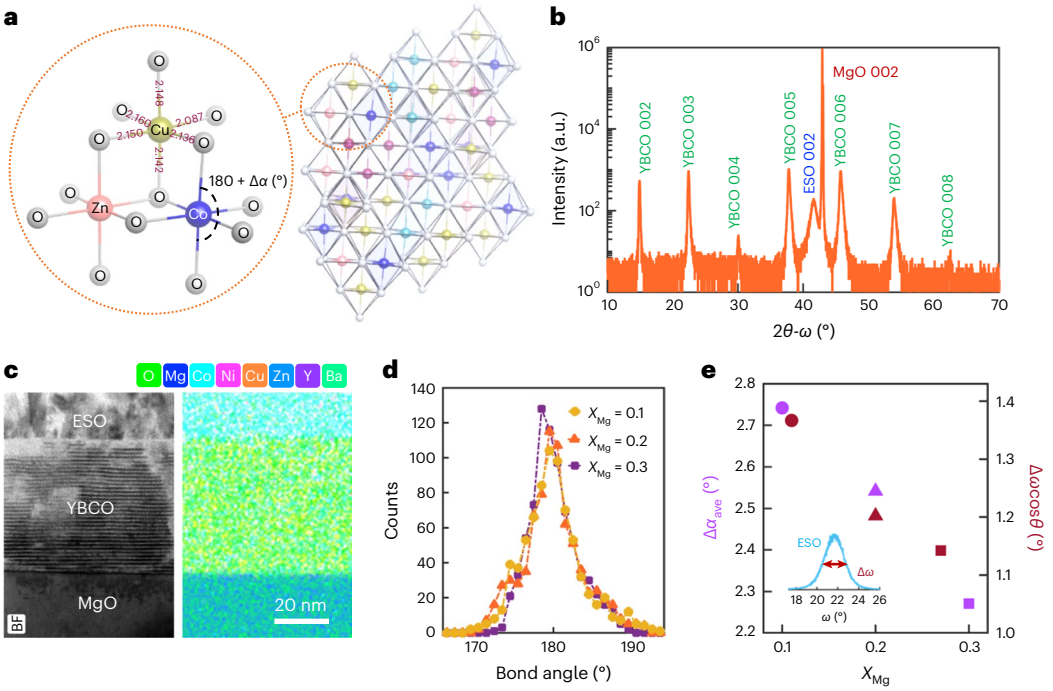

Fig. 1 | Tunable composition and structural disorder in single-crystalline ESO thin films on epitaxial YBCO electrodes. a, DFT-calculated atomic structure of (Mg,Co,Ni,Cu,Zn)O-type rocksalt ESO, highlighting the local distortions of the bond length and the deviation of the bond angle (α) from the ideal rocksalt structure. The variance is dominated by the Cu incorporation. **b**, X-ray diffraction pattern of an equimolar ESO/YBCO epitaxial bilayer on (001)-oriented MgO substrates. **c**, TEM and EDS elemental mapping images of the cross-section reveal sharp interfaces between the ESO/YBCO thin films. **d**, Histogram of anion–cation–anion bond angles for ESOs with varied Mg composition calculated from DFT. **e**, DFT-calculated average bond angle deviation, $\Delta\alpha_{ave}$, and the full-width half-maximum, $\Delta\omega\cos\theta$, of the X-ray diffraction rocking curve of ESO thin films decrease with increasing Mg composition, showing that the degree of structural distortion can be tuned by Mg composition. Inset: the raw data of the ESO (X_{Mg} = 0.20) rocking curve.

structural distortion. In particular, decreasing (increasing) magnesium composition increases (decreases) the vacancy concentration[26], resulting in the controlled tuning of hopping conductivity instead of stochastic filament formation processes. We use the ESO memristors to implement a reservoir computing (RC) network[11–13,15] that classifies time-series input data. Our experimental and computational results show that fine-tuning of switching dynamics can be achieved by adjusting the bulk properties of ESO-based memristors, and the tunability can be used to enhance computing performance.

Structure of ESO memristors

An epitaxial $YBa_2Cu_3O_{7-x}$ (YBCO) thin film is employed as the bottom electrode to fabricate epitaxial ESO metal–insulator–metal (MIM) structures and memristor devices. The details of the ESO/YBCO deposition on (001)-oriented MgO substrates and the fabrication of MIM structures are described in Methods. During growth, the structural disorder of the ESO film is tuned by adjusting the Mg concentration (X_{Mg} = 0.11, 0.20, 0.27 in $(Mg_xCo_{(1-x)/4}Ni_{(1-x)/4}Cu_{(1-x)/4}Zn_{(1-x)/4})O$).

The crystallinity and epitaxial relationship of multilayer thin films are characterized by X-ray measurements. Figure 1b shows X-ray diffraction measurements from a representative ESO (here X_{Mg} = 0.20)/YBCO bilayer sample. X-ray diffraction results for other Mg-variant ESO/YBCO thin films are shown in Supplementary Fig. 1, and the lattice parameter variation with Mg composition was found to be negligible in the range of X_{Mg} = 0.11–0.27. The YBCO layers are (001)-oriented and single phase. Despite the large misfit between the in-plane lattice parameters of ESO and YBCO (10.7% and 8.86% along the *a* and *b* directions, respectively), a strong ESO 002 X-ray diffraction peak is observed for all compositions, and no impurity peaks are detected. ESO films are 75 nm thick and strain-relaxed for all compositions. From asymmetric 022 and 026 peaks of the ESO and YBCO, respectively, the in-plane epitaxial relationship is determined as $[100]_{ESO}||[100]_{YBCO}$ (Supplementary Fig. 2). The in-plane orientation of the bilayers is further verified by the phi scans in Supplementary Fig. 3 that show fourfold symmetry of ESO 022 and YBCO 026 peaks.

Transmission electron microscopy (TEM) and energy-dispersive X-ray spectroscopy (EDS) studies were performed to investigate the composition and interface of the films (Fig. 1c). TEM reveals significant diffraction contrast consistent with relaxed films. Elemental mapping reveals a sharp interface for both ESO/YBCO and YBCO/MgO without noticeable diffusion (the mapping for each element is shown in Supplementary Fig. 4). The homogenous elemental distribution in ESO and YBCO layers verifies that the films are uniform without clear cluster formation or phase separation at the nanometre scale.

The tuning of ESO structural disorder by Mg composition is predicted by the structural relaxation from density functional theory (DFT) and then experimentally observed by the X-ray diffraction of our thin films. Among the binary oxides with the constituent cations forming the ESO film, MgO exhibits the rocksalt structure in the ground state with a lattice parameter close to that of the ESO. Therefore, increasing Mg composition is expected to reduce the structural distortion of ESO without significant changes of the lattice parameter. Figure 1d shows the calculated bond angle distribution of the ESO for different Mg compositions (X_{Mg} = 0.1, 0.2, 0.3) from DFT calculations (see Methods for calculation details). The calculated bond angle distribution of the ESO better matches the ideal rocksalt structure as X_{Mg} increases. X-ray diffraction rocking curves of the three ESO thin films show an evolution that is commensurate with the calculated structural disorder. Figure 1e plots the full-width half-maximum of the X-ray diffraction rocking curve ($\Delta\omega$) of the ESO thin films multiplied by $\cos\theta$, where θ is the diffraction peak, along with the DFT-calculated average bond angle deviation, $\Delta\alpha_{ave}$, of the ESO. Both $\Delta\omega\cos\theta$ and $\Delta\alpha_{ave}$ decrease with X_{Mg}, showing the compositional tuning of the structural distortion.

https://doi.org/10.1038/s41928-024-01169-1

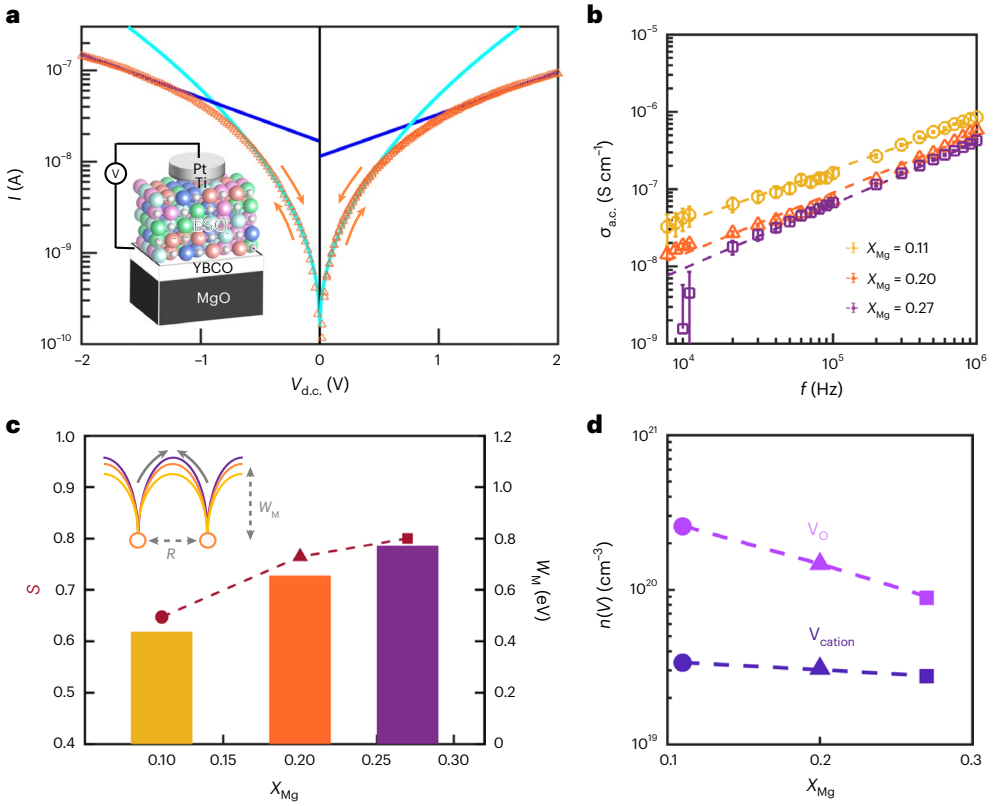

Fig. 2 | Tunable defect-mediated hopping conductivity in single-crystalline thin-film ESOs. a, The d.c. current–voltage sweeps of an ESO memristor (X_{Mg} = 0.20), with the curves fit by Schottky (cyan) and hopping conduction models (blue). No apparent threshold behaviour is observed, indicating the absence of the formation of conductive filaments. Inset: schematic of the ESO memristor stack. **b**, Frequency (f)-dependent conductivity ($\sigma_{a.c.}$) of ESO memristors at E = 133 kV cm^{-1} for three Mg concentrations. The measurement was performed with 15 devices for each composition, and data are presented as mean values with error bars defined by standard deviation. **c**, Fitted parameter s, from the power law given by $\sigma_{a.c.} \propto (2\pi f)^s$, and the energy barrier for hopping W_M, obtained by the CBH model[33], for the three Mg variants. Inset: the hopping barrier between defect sites. **d**, DFT-calculated cation and oxygen vacancy concentration as a function of Mg composition.

Tunable hopping conductivity

To evaluate the effects of composition tuning on the ESO film's electrical properties, MIM structure-based memristors using single-crystalline ESO films are fabricated (inset in Fig. 2a) using the YBCO film and Ti/Pt films as bottom and top electrodes, respectively; the high field electrode was the top electrode. The d.c. current (I)–voltage (V) sweeps of the ESO memristors reveal two dominant transport regimes, Schottky emission[27] ($\ln(I) \propto V^{1/2}$) at low electric field and hopping conduction[28] ($\ln(I) \propto V$) at high electric field (Fig. 2a). Notably, no apparent threshold behaviour is observed in the I–V curve for different sizes of electrodes from 200 nm to 60 µm (Supplementary Fig. 5), indicating the absence of the formation of conductive filaments.

The observed high field behaviour is consistent with defect-mediated hopping conduction by emptying and refilling the traps in the mid-gap states[28]. Due to the inherent structural disorder, ESO can accommodate a large amount of charged carriers associated with charged defects and multivalency of cations that contributes to hopping conduction[29,30]. Among native point defects, we determine that the majority of defects formed at our thermodynamic synthesis condition are V_O^{2+}, followed by V_{Cu}^{2-}, making Cu–O defect complexes the anticipated defect that mediates hopping[26]. To characterize the transport behaviour, frequency-dependent conductivity measurements were performed for all Mg concentrations under the bias of 1 V (hopping conduction) in Fig. 2b. The a.c. conductivity for all compositions can be well fit with a power-law equation:

$$\sigma_{a.c.} \propto (2\pi f)^s \ (s \leq 1) \tag{1}$$

From the fit, s parameters of 0.65 ± 0.11, 0.76 ± 0.08 and 0.80 ± 0.05 are obtained for X_{Mg} = 0.11, 0.20 and 0.27, respectively. These s values fall into the range that corresponds to hopping conduction[31], which is consistent with the I–V characteristics measurements and fitting results (Fig. 2a).

To obtain more information on the conduction mechanism, the data were analysed using the correlated barrier hopping (CBH) model, which describes the hopping of charge carriers through isolated trap pairs assuming a random distribution of traps. In the CBH model, the s parameter is related to the number of pairs that participate in hopping and can be expressed as[32]

$$s = 1 - \frac{6kT}{W_M} \tag{2}$$

where k is the Boltzmann constant, T is the absolute temperature and W_M is the maximum barrier height between two traps. W_M was calculated from the s parameters and plotted in Fig. 2c. The calculated W_M are 0.44 ± 0.15 eV, 0.66 ± 0.25 eV and 0.77 ± 0.19 eV for X_{Mg} = 0.11, 0.20 and 0.27, respectively, showing that increasing X_{Mg} enhances the barrier energy for hopping. The Mg-composition-dependent hopping barrier can be related to the DFT-calculated (0/+1) ionization energy of oxygen vacancy (E_i) (ref. 33). DFT predicts that E_i is dependent on local configuration, but the weighted average of E_i increases with Mg composition (E_i = 0.53 eV, 0.56 eV and 0.59 eV for X_{Mg} = 0.11, 0.20 and 0.27), which follows the experimental trend.

Throughout the measured frequency range ($f = 5 \times 10^3$ to 5×10^6 Hz), the conductivity of ESO memristors decreases as the

Mg composition increases, which is attributed to the decreased vacancy concentration of the ESO. Figure 2d shows the calculated oxygen and cation vacancy concentration as a function of Mg concentration, using the linear regression model of DFT-calculated vacancy formation energy obtained in ref. 26. Both oxygen and cation vacancies decrease with increasing Mg concentration, as more Mg leads to less local structural distortion and strain. To eliminate possible changes of the band gap as a factor, the band gap of each composition was computed and experimentally determined by absorption (Supplementary Fig. 6 and Methods). The result shows a small variation of the band gap with composition (within 0.1 eV). The Nyquist plot in Supplementary Fig. 7 presents a partial semicircle at high frequency (10^4 to 7×10^6 Hz) for all compositions, showing the presence of a charge-transfer mechanism and insulating behaviour of ESO thin films. Therefore, we conclude that the tunable conductivity of Mg-varied ESOs originates from the tuned vacancy concentration, where less Mg leads to more hopping sites for carriers.

Tunable RS characteristics

Next, pulse measurements were performed on the ESO memristors to investigate how the tunable hopping barrier height and defect concentration affect the memristors' RS dynamics and memory state. Specifically, defects due to oxygen vacancies in ESOs have deep energy levels in the mid gap. These defects are normally filled[5] and not accessible for newly injected electrons, and conduction through the device is through Schottky emission only, resulting in a high resistive state (HRS), as shown in Fig. 3a. At high applied voltage, electrons trapped in the defect levels escape from the traps, and these empty traps can facilitate hopping conduction of the injected electrons, leading to increased conductance (low resistive state (LRS)). After the bias is removed, it takes finite time (longer than the relaxation time (τ)) to refill the traps, leading to the observed short-term memory effect. The density of the traps is varied by the compositional difference, and the equilibrium Fermi level can be obtained by adapting the Fermi level pinning model as a function of oxygen potential, as discussed in ref. 32. For the experiment, pulse trains consisting of consecutive programming pulses and a read pulse are used, as shown in the inset of Fig. 3b. Details of the measurements can be found in Methods. Pulse trains with different time intervals ($t_{interval}$) between the programming pulses are also used to probe the internal dynamics of the ESO device with different Mg concentrations.

Figure 3b shows the results of the response to pulse trains with different $t_{interval}$ for the ESO devices with $X_{Mg} = 0.11$. The results of the ESO devices with $X_{Mg} = 0.20$ and 0.27 can be found in Supplementary Fig. 8. In all cases, a shorter $t_{interval}$ leads to a larger increase in the device conductance. This behaviour is consistent with previous studies on memristors with short-term memory[22,23] and can be explained by the interplay between the excitation caused by the programming pulses and gradual closing of the conduction channels due to the short-term memory effect between the pulses[11,12,22].

To test the capability of ESO-based memristors for temporal data processing beyond the simple pulse train, different combinations of pulses were used to measure the memristor's behaviour. Figure 3c depicts the memristor's conductance dynamics induced by the input pulse combinations illustrated in the top of each graph. As demonstrated in Fig. 3b and Supplementary Fig. 8, devices with different Mg concentrations show different responses to the temporally coded data. In general, conductance is enhanced by a programming pulse (input 1), whereas it relaxes towards the resting value in the absence of the pulse (input 0), and the overall device conductance depends not only on the number of programming pulses but also on their temporal locations. For example, in the (1,0,1,0) case, the conductance values after the first and third pulses are different, even though both pulses have a preceding 0 input. The higher conductance after the third pulse is caused by the remaining carriers excited by the first pulse that are not fully relaxed. As discussed in the previous studies[11,12,22], the short-term memory properties of the memristors allow the device to (nonlinearly) transform the temporal information into the different device states, where the information may be more efficiently processed in approaches such as RC. Area dependency of the conductance under the pulse inputs is also investigated and presented in Supplementary Fig. 9. The conductance of both HRS and LRS shows the area dependency.

The benefit of the ESO films studied here is that by tuning the Mg concentration, the short-term properties of the memristors can be systematically tuned, allowing a more diverse transformation and a larger reservoir state space. As can be seen in Fig. 3d, which plots the change in conductance ΔG (from post first pulse to post fourth pulse) as a function of $t_{interval}$ for the three Mg concentration cases. Smaller Mg concentration leads to a wider dynamic range of the conductance, as explained by the higher concentration of defects (Fig. 2d) that act as hopping sites. To further verify the role of oxygen vacancies, we post-annealed the ESO device at 100 mtorr O_2, 400 °C to compensate for the vacancies. The result shows that the dynamic range of the ESO is significantly suppressed, as shown in Supplementary Fig. 10.

The relaxation-time constants of the memristors were also characterized by the temporal dynamics of the conductance after programming. Fifty-five devices were measured in each Mg concentration using a pulse train of (1,0,0,0) (data shown in Supplementary Fig. 11), and the measured G versus time after the programming pulse was fitted with the stretched-exponential function[34,35]

$$G(t) = G_0 \exp[-(t/\tau)^{\beta}] \quad (3)$$

where $G(t)$ is the conductance, G_0 is the conductance just after programming, τ is the characteristic relaxation time and β is the stretch index representing the degree of disorder in the system[23]. The stretched-exponential function is commonly used to describe electronic or structural relaxation in disordered materials[34,36] and is used here to extract the relaxation time and measure the relative disorder from the temporal dynamics. Figure 3e shows the relaxation time and the stretch index of three devices from the stretched-exponential fitting. The results show that the electronic relaxation time increases with increasing Mg concentration, which is consistent with the extracted higher hopping energy barrier (W_M) (Fig. 2c) that prevents electrons trapped in the defects from escaping. The average of τ for $X_{Mg} = 0.11$, 0.20, 0.27 is 159 ± 6 ns, 199 ± 16 ns and 278 ± 2 ns (the ± reflects one standard deviation), respectively. The decrease in β with increasing Mg concentration is also consistent with results from Fig. 1e, which shows decreasing structural disorder with increasing Mg in the ESO. The average (with ± one standard deviation) of β for $X_{Mg} = 0.11$, 0.20, 0.27 is 0.215 ± 0.016, 0.188 ± 0.013, 0.153 ± 0.012, respectively.

Figure 3f shows endurance measurement results of the ESO-based memristors. The conductance of LRS and HRS was monitored after every 500 excitation/relaxation events. Stable switching behaviours with a standard deviation of 3.6% of the total average conductance and an On/Off ratio of 84 can be observed throughout the 1 million programming pulses. We also observe that the memristor behaviour is independent of background environment and the presence of water molecules, as shown in Supplementary Figs. 12 and 13. Supplementary Fig. 12 compares d.c. I–V curves and the conductance of LRS and HRS measured by the pulse trains obtained in dry N_2 and ambient conditions, and Supplementary Fig. 13 compares those of devices before and after heating at 100 °C in a vacuum.

ESO memristor-based RC

The fine-tunability of the device dynamics makes ESOs an excellent candidate for 'task-specific' neural network systems, which has remained challenging in amorphous oxides-based memristor devices due to the lack of tunability. In particular, the decaying time constant (relaxation time) has been widely used by various neural networks,

https://doi.org/10.1038/s41928-024-01169-1

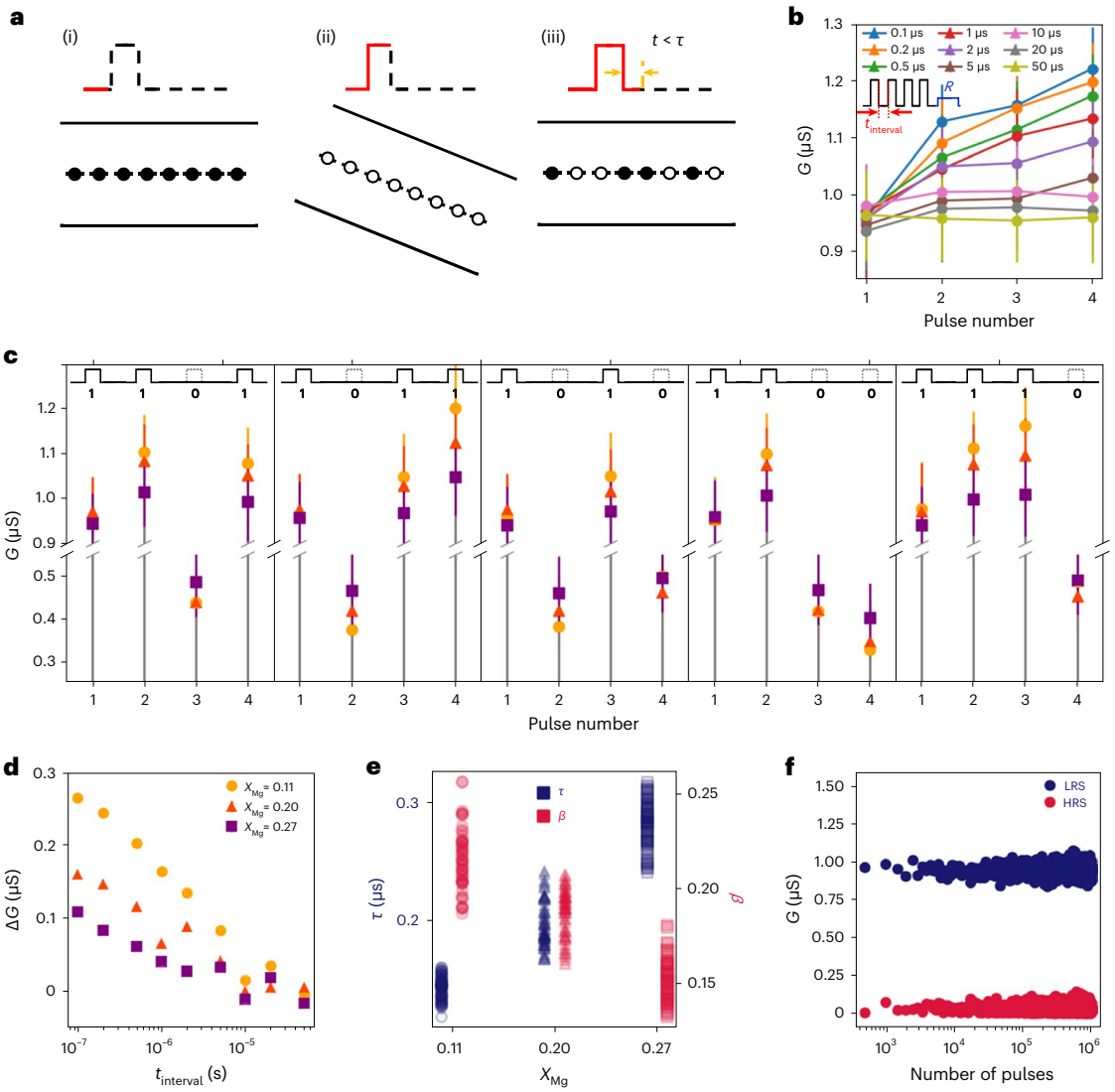

Fig. 3 | Tunable RS characteristics. a, Schematic of RS mediated by electrons trapping/detrapping in defects. (i) At low field, electrons are trapped in the deep-level defect sites caused by structural disorders in ESOs. The traps are not accessible for incoming electrons, and the conduction is dominated by Schottky emission, leading to a HRS. (ii) When a high electric field is applied, the traps become empty, which makes hopping conduction possible and leads to increase of conduction (LRS). (iii) Even if the field is removed, it takes finite time (τ) to refill the traps and re-establish the equilibrium state, leading to the short-term memory effect. **b**, Conductance changes induced by pulse trains with nine different time gaps ($t_{interval}$) between pulses (labelled in colours) on ESO-based memristors for $X_{Mg} = 0.11$. Each pulse train consists of four pulses with 2 V amplitude. The data were achieved 10 times for each time-gap condition on 55 devices per Mg concentration and are presented as mean values with error bars indicating standard deviation. **c**, Examples of conductance modulation caused by different input streams illustrated in the top of each graph, for the three types of memristor device. **d**, Effect of $t_{interval}$ on the excitation dynamic range for the three types of memristor devices. **e**, Decay time constant t and stretch index β as a function of Mg concentration. **f**, Endurance test for the device with $X_{Mg} = 0.11$ composition. The conductance was measured after every 500 excitation/relaxation events.

where each network may require an optimal time constant for the best performance. Examples include the leaky term of a leaky integrate and fire neuron[37], time context in a time surface[38] and reservoir nodes in RC systems[11,12,15]. In a leaky integrate and fire neuron circuit that accumulates the potential and produces a spike when the potential exceeds its threshold, ESOs can replace a resistor/capacitor in reducing/accumulating the potential with improved energy efficiency and area density[39].

RC systems are another class that have gained interest in efficient temporal data processing. An RC network uses the nonlinear transformation function of the reservoir to map an input vector into a high-dimensional computational space (the reservoir state)[12,40]. Key to RC performance is the ability of the reservoir to offer diverse temporal dynamics to map temporal data (such as pulse trains representing time-series data) onto the reservoir state, and the tunability of internal time constants in the ESO film helps the implementation of such reservoirs.

To verify how the tunability of ESO memristors can improve RC system performance, a spoken-digit recognition test was performed using physically implemented ESO memristor-based reservoir hardware and the architecture depicted in Fig. 4a. For the time-series dataset, Audio-MNIST[41] was used, and an example of the dataset is shown in Fig. 4b. Each input is 64 time steps long. Following the cochlear ear model[42], the input data are translated into spikes from 64 frequency channels. A pulse (spike) is generated whenever the intensity exceeds a pre-fixed threshold in each channel. In the experimental setup, input pulses from each channel are applied to a memristor, such as $M_1, M_2, \ldots, M_n$, where the collection of memristors form a reservoir. Three different physical RC systems were fabricated. Each physical RC system includes 64 ESO memristors with a certain

https://doi.org/10.1038/s41928-024-01169-1

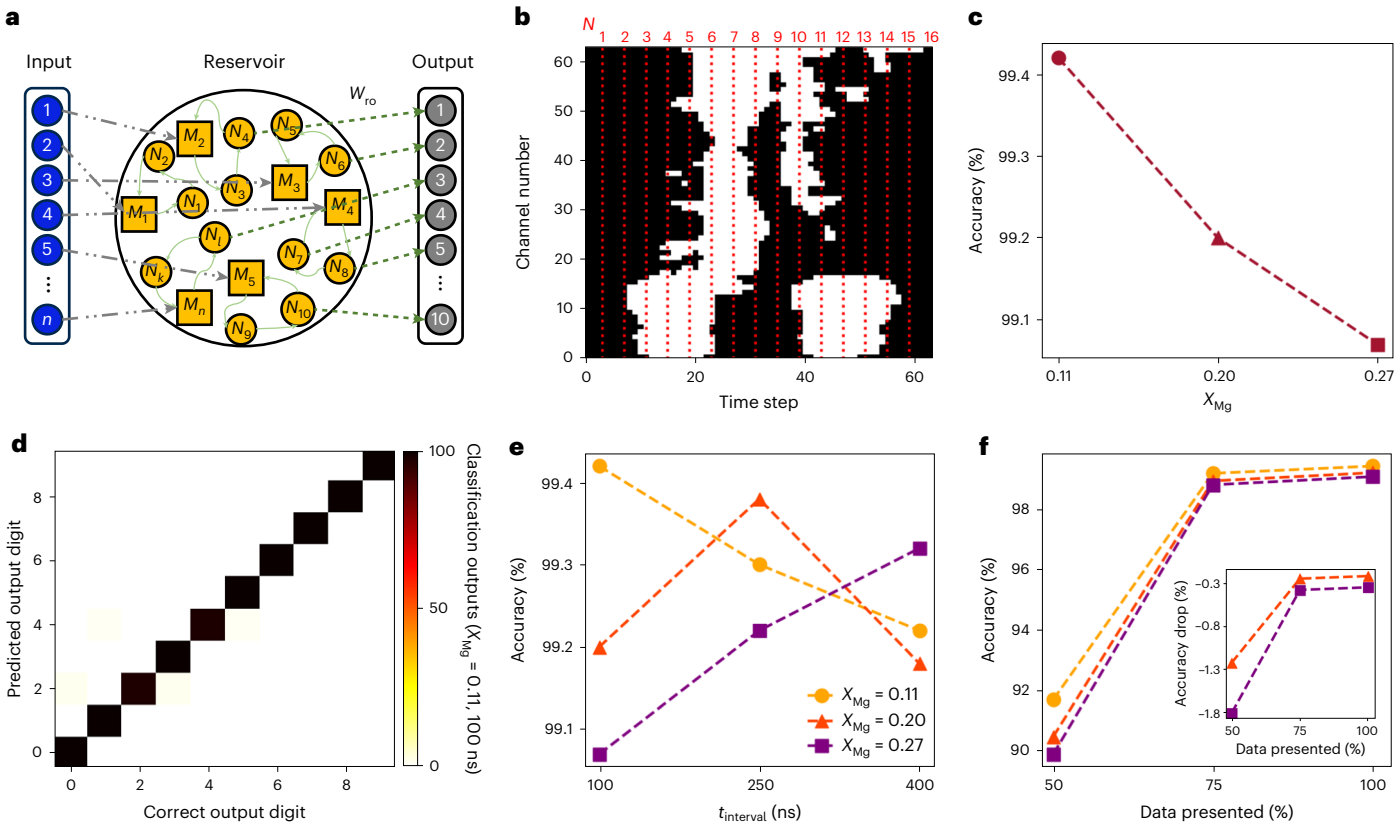

Fig. 4 | Experimentally implemented RC network with ESO memristors. **a**, Network configuration for the RC system, showing an input layer, a reservoir comprising ESO memristors and a readout layer with trainable weights W_{ro}. **b**, An example in the spoken-digit dataset. The spikes are represented in white. Red dotted lines show the division into virtual nodes. **c**, Performance of reservoir systems made of the three types of ESO memristor on inputs with 100 ns time-step interval. **d**, Experimentally obtained confusion matrix representing the classification outputs from the RC hardware system using ESOs with X_{Mg} = 0.11 for the 100 ns time interval test. **e**, Accuracy comparison of three RC systems on inputs with 100, 250, 400 ns time-step intervals, respectively. **f**, Prediction accuracy of the three RC systems at different percentages of inputs. Inset: the accuracy drop for systems with X_{Mg} = 0.20 and 0.27 compared with the X_{Mg} = 0.11 system, at different incomplete input levels.

cation composition. Each memristor in an RC system is individually connected to an input channel. No interconnection and data transportation are needed between the memristors. The concept of virtual nodes was adopted to divide the inputs into segments[43] and record the memristor states at the end of each segment as a virtual node of the reservoir. In this study, 16 virtual nodes (N_1, N_2, ..., N_k) were adopted per memristor: that is, the memristor conductance is read every four time steps[43]. Consequently, the total number of virtual nodes in the reservoir is 64 × 16. The experimentally recorded memristor states are then sent to the readout layer, which is a simple fully connected layer with 64 × 16 inputs and ten outputs implemented in Python. In the RC system, only the readout layer is trained. A detailed description of the RC operation and readout layer training can be found in Methods.

Memristors with different internal time constants allow the right device to be engineered for different applications. Figure 4c shows results from the three different RC systems for the Audio-MNIST test, using ESO memristors of a kind with Mg concentrations of X_{Mg} = 0.11, 0.20, 0.27, respectively. All RC systems have the same structure, and the inputs are applied at 100 ns intervals between time steps. All three systems produced very high classification accuracy, suggesting the ESO memristors are excellent candidates for RC systems. The RC network with X_{Mg} = 0.11 shows the best accuracy of 99.42% among the three systems, because the internal time constant of these memristors (~100 ns) better matches the inputs. The confusion matrix of the classification outputs for the X_{Mg} = 0.11 memristor system is shown in Fig. 4d, showing high classification accuracy for all input digits.

When the input time-step interval is increased, corresponding to inputs with longer temporal features, the responses from the RC systems changed accordingly (Fig. 4e). As the input time step is increased to 250 and 400 ns, the performance of the RC system with X_{Mg} = 0.11 decreases, whereas that of the RC systems with X_{Mg} = 0.20 and 0.27 increases. The X_{Mg} = 0.20 system reaches the highest accuracy when the input time step interval is 250 ns and starts to decrease again, while the X_{Mg} = 0.27 system reaches the highest accuracy at the longest input time-step interval of 400 ns. The ability to tune the internal time constants of the ESO memristors suggests the feasibility of engineering devices and RC systems to optimally match given tasks.

Figure 4f shows the capability of the RC system to predict of the digit before completing the utterance: that is, classification using incomplete input data[12]. In this test, after training the network with the standard dataset, the network output is measured using partial input data for the spoken digits. Figure 4f shows that for 100 ns time-step inputs, the RC system based on memristors with X_{Mg} = 0.11 still produces acceptable performance (>91.7% accurate) with only 50% inputs. RC systems based on memristors with X_{Mg} = 0.20 and X_{Mg} = 0.27 show worse performance for this input scale, and the degradation in accuracy becomes more severe as the input becomes more incomplete.

Energy consumption for the nonlinear transformation in the RC experiment was calculated using the experimentally implemented spike and read pulses and the measured conductance values from a reservoir of ESOs with X_{Mg} = 0.11. The current/voltage values measured by read pulses were used for the calculation of read operations, and the averaged measured conductance value was used to calculate

https://doi.org/10.1038/s41928-024-01169-1

Table 1 | Comparison of energy consumption to generate a signal spike on different systems

	CPU[12]	FPGA[12]	Memristor				
			WO_x (ref. 12)	NbO_x (ref. 44)	B-Te (ref. 44)	HfO_2 (ref. 44)	ESO
Energy per spike	54.8 µJ	143 nJ	3 nJ	50 pJ	30 pJ	20 pJ	3.39 pJ

CPU, central processing unit; FPGA, field-programmable gate array.

currents induced by spikes. The energy consumed per spike is 3.39 pJ, and the total energy consumption during testing of 600 spoken digits is 8.81 µJ. Compared with other systems using the numerical differential equation solvers in central processing units and field-programmable gate arrays or physical dynamics of other memristors[12,44], the ESO-based reservoir consumed one order of magnitude lower energy per input than the state of the art, for the similar usages as presented in Table 1.

Conclusions

We have reported the development of ESO memristors. Through composition control, tunable local structural disorder can be formed in the devices, which leads to stable and tunable switching dynamics. We used the ESO-based memristors to form RC networks, with the controllability of the internal time constants allowing matched reservoirs to be engineered for tasks such as spoken-digit recognition and prediction at different time scales. The temporal dynamics of ESO memristors, and their predictable tuning parameters, make them a promising system for use in efficient spatiotemporal data-processing applications.

Methods

Fabrication of ESO memristors

Single-crystal ESO films were grown on (001)-oriented MgO substrates by pulsed laser deposition using a 248 nm KrF excimer laser and stoichiometric targets. ESO targets were prepared by mixing the constituent powders (MgO (Alfa Aesar 99.99%), CoO (Alfa Aesar 99.99%), NiO (Alfa Aesar 99.99%), CuO (Alfa Aesar, 99.99%) and ZnO (Alfa Aesar, 99.99%)), pressing the mixture of powders under 50,000 psi and sintering at 1,000 °C for 24 hours in air. YBCO targets were prepared by mixing the raw powders Y_2O_3 (Alfa Aesar 99.995%), $BaCO_3$ (Alfa Aesar 99.95%) and CuO (Alfa Aesar, 99.99%) in a ratio of Y:Ba:Cu = 1:2:3 using the reaction $0.5(Y_2O_3) + 2(BaCO_3) + 3(CuO) \rightarrow YBa_2Cu_3O_{7-x} + 2(CO_2)$. This mixture was thoroughly mixed with an agate mortar and pestle, reground by ball milling and placed in an Al_2O_3 crucible. First a calcination step was performed in a tube furnace at 920 °C in air for 24 hours. After cooling to room temperature, the black powder was reground using an agate mortar and pestle and then pressed under pressure of 12,000 psi into a 2-inch-diameter pellet. The sintering step was carried out at 940 °C for 48 hours. Cooling after the last sintering step and the subsequent oxygen heat treatment were performed in an oxygen atmosphere.

Before film deposition, the MgO substrate was pre-annealed at 950 °C in 50 mtorr of O_2 for 30 min to remove hydroxides on the substrate surface. To deposit the YBCO bottom electrode, the substrate was cooled to 850 °C, and the O_2 pressure was increased to 100 mtorr. The laser was directed onto the YBCO target with a fluence of 2 J cm^{-2} and a repetition frequency of 5 Hz. After 30 min of deposition, 50-nm-thick YBCO thin films were obtained. An ESO film of the desired composition was subsequently deposited on the YBCO layer at a substrate temperature of 400 °C and pressure of 5 mtorr of O_2 using the same laser fluence and 2 Hz rep rate. After 2 hours of deposition, 5-nm-thick ESO films were obtained. After growth, the substrates were slowly cooled to room temperature under 100 sccm O_2 flow (~500 mtorr).

After deposition of the ESO/YBCO bilayers, circular top contacts ranging in diameter from 15 to 130 µm were patterned on the surface using standard photolithography and lift-off processes. Top contacts of Pt(100 nm)/Ti(2 nm) were deposited at room temperature by pulsed laser deposition in 10 mtorr Ar with a laser fluence of 3 J cm^{-2} and a repetition frequency of 5 Hz.

DFT calculation of ESOs with varied Mg incorporation

DFT calculations were performed to calculate the structural distortion and band gap of Mg-variant ESOs. The projector augmented wave method and generalized gradient approximation functionals were implemented in the Vienna Ab initio Simulation Package[45] with a Hubbard U parameter[46] assigned for the transition metal cations. The same pseudopotential, plane-wave cut-off energy, energy criterion for electronic relaxation, ionic relaxation algorithm, force criterion for ionic relaxation and Hubbard U parameters were used for the calculation of ESO in ref. 26.

One hundred and sixty atom supercells of ESOs with three different compositions were modelled: $Mg_{0.1}Co_{0.225}Ni_{0.225}Cu_{0.225}Zn_{0.225}O$, $Mg_{0.2}Co_{0.2}Ni_{0.2}Cu_{0.2}Zn_{0.2}O$ and $Mg_{0.3}Co_{0.175}Ni_{0.175}Cu_{0.175}Zn_{0.175}O$. The alloy randomness was modelled using special quasi-random structures[47]. The antiferromagnetic structure of the ESO[48] was considered by equally populating each cation in the two magnetic states. The lattice constant was determined by the energy minimum and was only varied with Mg composition by <0.01 Å, which agrees with our X-ray diffraction data. The *k*-point sampling for the supercell is Γ-centred 2 × 2 × 1 in the first Brillouin zone. The band gap was calculated at the Γ point.

Band-gap measurement of ESO thin films

The band gap (E_g) of Mg-varied ESO thin films was determined from epitaxial films deposited on bare MgO substrates with the same deposition conditions used for ESO deposition on YBCO-buffered MgO substrates. The optical transmittance of Mg-variant ESO thin films was measured (Supplementary Fig. 6a). To evaluate optical E_g, the difference between the measured absorbance of ESO thin films on MgO and that of a bare MgO substrate was taken. A Tauc plot (Supplementary Fig. 6b) reveals a linear relation for $(ah\nu)^2$ versus $h\nu$ (a, absorption coefficient; h, Planck's constant; ν, frequency of light; $h\nu$, photon energy), which indicates an indirect transition. The obtained band gap of the ESO (Supplementary Fig. 6c) is almost constant for the different Mg compositional variants (E_g = 2.55 eV, 2.58 eV and 2.60 eV for X_{Mg} = 0.11, 0.20 and 0.27, respectively). The Urbach tail was excluded from the fit.

Pulse measurement of ESO-based memristors

All pulse measurements were performed on the MIM stacks (described previously) using a Keithley 4200S semiconductor analyser. Programming pulses with an amplitude of 2 V and pulse width of 1 ms and read pulses with an amplitude of 0.3 V and pulse width of 10 ms were used. The pulses were applied to the top electrode of the MIM stack as shown in the inset of Fig. 3a. The time gap between the last programming pulse of a series of programming pulses and the read pulse was set to be 100 ns, and the gap between programming pulses was varied as intended. Nine different time gaps were tested in total. To minimize effects from noise and device variations, the measurements were performed ten times for each time-gap condition on 55 devices per Mg concentration.

RC using ESO-based memristors

The first 3,000 data of the Audio-MNIST dataset were chosen for the RC experiment. The data inputs were binarized by the pre-fixed threshold value of 0.4 to convert normalized inputs to spike trains. The amplitude and width of the spikes and the read pulse were identical to those used for the standalone pulse measurements discussed earlier. The spike train from each channel was applied to a separate ESO-based

memristor, and its conductance was monitored every four spikes (corresponding to 16 virtual nodes) experimentally. The conductance history of 64 devices, representing 64 channels for the data per Mg concentration, was recorded.

After the experimental encoding and recording of the ESO memristor in the reservoir, the computation simulation is followed to perform the speech-recognition task using the experimental data. The readout function is a 64 × 16 × 10 network with ten outputs representing ten different digits in the case of a RC system with a reservoir. It takes the recorded conductance values as inputs (64 × 16) and outputs ten outputs using the input vector and its weight matrix. The probability of an output neuron being chosen as the classification result was calculated by a SoftMax function, and the neuron with the largest possibility was selected. The cost was derived by categorical cross-entropy[12] and RMSprop was used for optimization skill[49]. Eighty per cent of the recorded data were used for training the readout function and the rest were used for testing the network[12].

Data availability

Source data are provided with this paper. Additional data related to this work are available from the corresponding authors upon request.

Code availability

Computational simulation code of the RC system for the speech-recognition task is available from the corresponding authors upon reasonable request.

References

1. Kumar, S., Wang, X., Strachan, J. P., Yang, Y. & Lu, W. D. Dynamical memristors for higher-complexity neuromorphic computing. *Nat. Rev. Mater.* **7**, 575–591 (2022).
2. Zidan, M. A. et al. A general memristor-based partial differential equation solver. *Nat. Electron* **1**, 411–420 (2018).
3. Prezioso, M. et al. Training and operation of an integrated neuromorphic network based on metal-oxide memristors. *Nature* **521**, 61–64 (2015).
4. Strukov, D. B., Snider, G. S., Stewart, D. R. & Williams, R. S. The missing memristor found. *Nature* **453**, 80–83 (2008).
5. Zidan, M. A., Strachan, J. P. & Lu, W. D. The future of electronics based on memristive systems. *Nat. Electron.* **1**, 22–29 (2018).
6. Cai, F. et al. A fully integrated reprogrammable memristor–CMOS system for efficient multiply–accumulate operations. *Nat. Electron.* **2**, 290–299 (2019).
7. Chen, S. et al. Wafer-scale integration of two-dimensional materials in high-density memristive crossbar arrays for artificial neural networks. *Nat. Electron.* **3**, 638–645 (2020).
8. Yao, P. et al. Fully hardware-implemented memristor convolutional neural network. *Nature* **577**, 641–646 (2020).
9. Yin, S. et al. Monolithically integrated RRAM- and CMOS-based in-memory computing optimizations for efficient deep learning. *IEEE Micro* **39**, 54–63 (2019).
10. Liu, Q. et al. 33.2 A fully integrated analog ReRAM based 78.4TOPS/W compute-in-memory chip with fully parallel MAC computing. In *Proc. 2020 IEEE International Solid-State Circuits Conference* (eds Fujino, L. C. et al.) 500–502 (IEEE, 2020).
11. Du, C. et al. Reservoir computing using dynamic memristors for temporal information processing. *Nat. Commun.* **8**, 2204 (2017).
12. Moon, J. et al. Temporal data classification and forecasting using a memristor-based reservoir computing system. *Nat. Electron.* **2**, 480–487 (2019).
13. Moon, J., Wu, Y. & Lu, W. D. Hierarchical architectures in reservoir computing systems. *Neuromorphic Comput. Eng.* **1**, 014006 (2021).
14. Yoo, S. et al. Columnar learning networks for multisensory spatiotemporal learning. *Adv. Intell. Syst.* **4**, 2200179 (2022).
15. Yoo, S., Lee, E. Y.-J., Wang, Z., Wang, X. & Lu, W. D. RN-Net: reservoir nodes-enabled neuromorphic vision sensing network. Preprint at http://arxiv.org/abs/2303.10770 (2023).
16. Li, Y., Wang, Z., Midya, R., Xia, Q. & Yang, J. J. Review of memristor devices in neuromorphic computing: materials sciences and device challenges. *J. Phys. D* **51**, 503002 (2018).
17. Lee, J. & Lu, W. D. On-demand reconfiguration of nanomaterials: when electronics meets ionics. *Adv. Mater.* **30**, 1702770 (2018).
18. Lee, S. H. et al. Quantitative, dynamic TaO_x memristor/resistive random access memory model. *ACS Appl. Electron. Mater.* **2**, 701–709 (2020).
19. Kim, S. et al. Experimental demonstration of a second-order memristor and its ability to biorealistically implement synaptic plasticity. *Nano Lett.* **15**, 2203–2211 (2015).
20. Yoo, S., Wu, Y., Park, Y. & Lu, W. D. Tuning resistive switching behavior by controlling internal ionic dynamics for biorealistic implementation of synaptic plasticity. *Adv. Electron. Mater.* **8**, 2101025 (2022).
21. Kumar, S., Williams, R. S. & Wang, Z. Third-order nanocircuit elements for neuromorphic engineering. *Nature* **585**, 518–523 (2020).
22. Du, C., Ma, W., Chang, T., Sheridan, P. & Lu, W. D. Biorealistic implementation of synaptic functions with oxide memristors through internal ionic dynamics. *Adv. Funct. Mater.* **25**, 4290–4299 (2015).
23. Chang, T., Jo, S. & Lu, W. Short-term memory to long-term memory transition in a nanoscale memristor. *ACS Nano* **5**, 7669–7676 (2011).
24. Rost, C. M. et al. Entropy-stabilized oxides. *Nat. Commun.* **6**, 8485 (2015).
25. Meisenheimer, P. B. et al. Magneticfrustration control through tunable stereochemically driven disorder in entropy-stabilized oxides. *Phys. Rev. Mater.* **3**, 104420 (2019).
26. Chae, S., Williams, L., Lee, J., Heron, J. T. & Kioupakis, E. Effects of local compositional and structural disorder on vacancy formation in entropy-stabilized oxides from first-principles. *npj Comput. Mater.* **8**, 95 (2022).
27. Sze, S. M. & Ng, K. K. *Physics of Semiconductor Devices* 3rd edn (Wiley, 2007).
28. Ielmini, D. & Zhang, Y. Analytical model for subthreshold conduction and threshold switching in chalcogenide-based memory devices. *J. Appl Phys.* **102**, 054517 (2007).
29. Kotsonis, G. N. et al. Property and cation valence engineering in entropy-stabilized oxide thin films. *Phys. Rev. Mater.* **4**, 100401 (2020).
30. Jacobson, V. et al. The role of co valence in charge transport in the entropy-stabilized oxide (Mg0.2Co0.2Ni0.2Cu0.2Zn0.2)O. *J. Am. Ceram. Soc.* **106**, 1531–1539 (2023).
31. Schrøder, T. B. & Dyre, J. C. Universality of AC conduction in disordered solids. *Rev. Mod. Phys.* **72**, 873–892 (2000).
32. Elliott, S. R. A.C. conduction in amorphous chalcogenide and pnictide semiconductors. *Adv. Phys.* **36**, 135–218 (1987).
33. Lee, J., Lu, W. D. & Kioupakis, E. Electronic and optical properties of oxygen vacancies in amorphous Ta_2O_5 from first principles. *Nanoscale* **9**, 1120–1127 (2017).
34. Phillips, J. C. Stretched exponential relaxation in molecular and electronic glasses. *Rep. Prog. Phys.* **59**, 1133–1207 (1996).
35. Wu, Z. W., Kob, W., Wang, W. & Xu, L. Stretched and compressed exponentials in the relaxation dynamics of a metallic glass-forming melt. *Nat. Commun.* **9**, 5334 (2018).
36. Scher, H., Shlesinger, M. F. & Bendler, J. T. Time-scale invariance in transport and relaxation. *Phys. Today* **44**, 26–34 (1991).
37. Park, S.-O., Jeong, H., Park, J., Bae, J. & Choi, S. Experimental demonstration of highly reliable dynamic memristor for artificial neuron and neuromorphic computing. *Nat. Commun.* **13**, 2888 (2022).

38. Lagorce, X., Orchard, G., Galluppi, F., Shi, B. E. & Benosman, R. B. HOTS: a hierarchy of event-based time-surfaces for pattern recognition. *IEEE Trans. Pattern Anal. Mach. Intell.* **39**, 1346–1359 (2017).
39. Wu, X., Saxena, V., Zhu, K. & Balagopal, S. A CMOS spiking neuron for brain-inspired neural networks with resistive synapses and in-situ learning. *IEEE Trans. Circuits Syst. II* **62**, 1088–1092 (2015).
40. Gauthier, D. J., Bollt, E., Griffith, A. & Barbosa, W. A. S. Next generation reservoir computing. *Nat. Commun.* **12**, 5564 (2021).
41. Becker, S., Ackermann, M., Lapuschkin, S., Müller, K.-R. & Samek, W. Interpreting and explaining deep neural networks for classification of audio signals. *J. Frank. Inst.* **361**, 418–428 (2024).
42. Lyon, R. A computational model of filtering, detection, and compression in the cochlea. In *Proc. IEEE International Conference on Acoustics, Speech, and Signal Processing* (eds Dixon, N. R. et al.) 1282–1285 (IEEE, 1982).
43. Appeltant, L. et al. Information processing using a single dynamical node as complex system. *Nat. Commun.* **2**, 468 (2011).
44. Lee, D. et al. Various threshold switching devices for integrate and fire neuron applications. *Adv. Electron. Mater.* **5**, 1800866 (2019).
45. Kresse, G. & Furthmüller, J. Efficiency of ab-initio total energy calculations for metals and semiconductors using a plane-wave basis set. *Comput. Mater. Sci.* **6**, 15–50 (1996).
46. Anisimov, V. I., Zaanen, J. & Andersen, O. K. Band theory and Mott insulators: Hubbard U instead of Stoner I. *Phys. Rev. B* **44**, 943–954 (1991).
47. Van De Walle, A. et al. Efficient stochastic generation of special quasirandom structures. *CALPHAD* **42**, 13–18 (2013).
48. Zhang, J. et al. Long-range antiferromagnetic order in a rocksalt high entropy oxide. *Chem. Mater.* **31**, 3705–3711 (2019).
49. Paszke, A. et al. PyTorch: an imperative style, high-performance deep learning library. In *Proc. Advances in Neural Information Processing Systems* (eds Wallach, H. et al.) 8024–8035 (NeurIPS, 2019).

Acknowledgements

This work was supported by the National Science Foundation (NSF) through awards CCF-1900675, ECCS-1915550, NSF CAREER grant no. DMR-1847847 and NSF MRSEC grant no. DMR-2011839, S.C. acknowledges support from Rackham Predoctoral Fellowship. We gratefully acknowledge the Michigan Center for Materials Characterization. We also acknowledge technical support from Lurie Nanofabrication Facility.

Author contributions

S.Y. and S.C. conceived the idea and designed the experiments. S.C. synthesized the materials and fabricated the devices under J.T.H.'s supervision together with T.C. S.C. performed the TEM, EDS and material characterizations with T.M., H.P., K.N. and H.G.X. S.C. performed the DFT calculation with L.W. under E.K.'s supervision. S.Y. performed the pulse measurements and analysis with Y.P. and demonstrated the RC systems under W.D.L.'s supervision. S.Y. and S.C. wrote the paper under the supervision of W.L. and J.T.H. All authors contributed to the discussion and checked the paper.

Competing interests

The authors declare no competing interests.

Additional information

Supplementary information The online version contains supplementary material available at https://doi.org/10.1038/s41928-024-01169-1.

Correspondence and requests for materials should be addressed to John T. Heron or Wei D. Lu.

Peer review information *Nature Electronics* thanks Shriram Ramanathan, Cristina Rost and Ilia Valov for their contribution to the peer review of this work.